Biomed Microdevices (2015) 17: 17
DOI 10.1007/s10544-014-9905-x

Microfluidic filtration and extraction of pathogens from food samples by hydrodynamic focusing and inertial lateral migration

Liviu Clime · Xuyen D. Hoa · Nathalie Corneau · Keith J. Morton · Christian Luebbert · Maxence Mounier · Daniel Brassard · Matthias Geissler · Sabah Bidawid · Jeff Farber · Teodor Veres

Published online: 1 February 2015

Abstract Detecting pathogenic bacteria in food or other biological samples with lab-on-a-chip (LOC) devices requires several sample preparation steps prior to analysis which commonly involves cleaning complex sample matrices of large debris. This often underestimated step is important to prevent these larger particles from clogging devices and to preserve initial concentrations when LOC techniques are used to concentrate or isolate smaller target microorganisms for downstream analysis. In this context, we developed a novel microfluidic system for membrane-free cleaning of biological samples from debris particles by combining hydrodynamic focusing and inertial lateral migration effects. The microfluidic device is fabricated using thermoplastic elastomers being compatible with thermoforming fabrication techniques leading to low-cost single-use devices. Microfluidic chip design and pumping protocols are optimized by investigating diffusive losses numerically with coupled Navier–Stokes and convective-diffusion theoretical models. Stability of inertial lateral migration and separation of debris is assessed through fluorescence microscopy measurements with labelled particles serving as a model system. Efficiency of debris cleaning is experimentally investigated by monitoring microchip outlets with *in situ* optical turbidity sensors, while retention of targeted pathogens (i.e., *Listeria monocytogenes*) within the sample stream is assessed through bacterial culture techniques. Optimized pumping protocols can remove up to 50 % of debris from ground beef samples while percentage for preserved microorganisms can account for 95 % in relatively clean samples. However, comparison between inoculated turbid and clean samples (i.e., with and without ground beef debris) indicate some degree of interference between debris inertial lateral migration and hydrodynamic focusing of small microorganisms. Although this interference can lead to significant decrease in chip performance through loss of target bacteria, it remains possible to reach 70 % for sample recovery and more than 50 % for debris removal even in the most turbid samples tested. Due to the relatively simple design, the robustness of the inertial migration effect itself, the high operational flow rates and fabrication methods that leverage low-cost materials, the proposed device can have an impact on a wide range of applications where high-throughput separation of particles and biological species is of interest.

Keywords Inertial microfluidics · Hydrodynamic focusing · Microfluidic filtration · Sample preparation · Hot embossing · Food safety inspection

L. Clime · X. D. Hoa · K. J. Morton · M. Mounier · D. Brassard · M. Geissler · T. Veres (✉)
National Research Council of Canada, 75 Boulevard de Mortagne, Boucherville, QC J4B 6Y4, Canada
e-mail: Teodor.Veres@cnrc-nrc.gc.ca

N. Corneau · C. Luebbert · S. Bidawid · J. Farber
Bureau of Microbial Hazards, Health Canada, 251 Sir Frederick Banting Driveway, Ottawa, ON K1A 0K9, Canada

1 Introduction

Lab-on-a-chip (LOC) systems offer the prospect of increased analytical throughput while reducing sample consumption, manual intervention and risks of contamination for a variety of applications that may include food safety inspection, clinical diagnostics, and environmental monitoring, among others. While their capacity has been demonstrated in a number of ways (Madou et al. 2006; Mark et al. 2010; Neethirajan et al. 2011), the widespread use of LOC devices in routine, real-life applications is yet to become a reality (Escarpa 2014). A major challenge in this context is the diverse nature and constitution of samples which often contain low amounts of

analyte in a complex matrix (e.g., food, natural water or soil). Up-front sample preparation hence constitutes an essential part of the overall analysis process which often involves both purification and separation of target species (Geissler et al. 2012; Isabel et al. 2012; Lim et al. 2005). Separation of analyte (e.g., bacteria or DNA) improves signal-to-noise ratios by increasing target concentrations, while cleaning steps are used to remove debris or other contaminants that may impede proper sensor function or even clog downstream LOC microfluidic components. The key task in "sample-to-answer" applications is to design devices capable of actively selecting target species by leveraging specific physical properties that differentiate them from the surrounding sample matrices.

One of the most popular and simple sample preparation techniques for cleaning and concentration is size-based membrane filtration (Wei et al. 2011). Porous filters are used to separate samples into two fractions: the retentate, which is immobilized on the membrane and the permeate, containing the suspension of particles smaller than the pore size. Sequential filtration and re-suspension steps can be used to refine separation until the desired concentration or sample purity is obtained. However, accumulation of debris can be problematic as it can cause clogging of the filter unit especially in very turbid and large-volume samples. Using filters with a large surface area or pump protocols for re-opening the pores can redress this issue, but loss of analyte due to non-specific adsorption can also become significant. Moreover, integration of porous membranes within microfluidic chips requires additional fabrication steps and thus increases chip complexity and cost.

Alternative approaches for sample preparation based on centrifugation (Leung 2007), dielectrophoresis (Lapizco-Encinas et al. 2004), acoustic trapping (Kuznetsova and Coakley 2007) and magnetic confinement(Clime et al. 2008) have been reported in the literature. While of interest to capture and concentrate specific target species, these approaches are limited to working with pre-cleaned samples from which larger debris has already been removed. Many of these approaches also rely on specific physical properties of the target species, and, in addition, require more complex fabrication schemes along with electronic controls for the manipulation of the necessary electrical, magnetic and acoustic fields.

Recently, a new method for sorting particles and cells (Di Carlo 2009) has emerged based on the inertial focusing effect (Saffman 1965; Saffman 1968; Segre and Silberberg 1961). Unlike alternative approaches that rely on additional physical properties of the targeted particles such as mass, density, electric polarizability or magnetic moment, this new method is based solely on the size of the particles themselves and the velocity profile of the carrier flow. Particles ranging from few hundred nanometers up to several tens of micrometers are of great interest in many biological applications. Within the theoretical framework of the inertial effect, to accommodate this range of particles, devices featuring fluidic channels of critical sizes from few microns up to several hundreds of microns in width are necessary (Bhagat et al. 2009; Di Carlo 2009; Segre and Silberberg 1961). This match between biological and microfluidic length scales provided a new driver for microfluidics research, triggering the topic of inertial microfluidics (Di Carlo 2009) that deals with the fundamental physics of the inertial focusing effect and its application to biological and medical research.

To this end, the inertial focusing effect has recently been demonstrated for sample preparation in LOC devices (Nieuwstadt et al. 2011) where target particles from a sample stream flowing at the centre of a microfluidic channel are transferred laterally into a clean, co-flowing buffer liquid. Furthermore, novel approaches to hydrodynamically focus multiple component flows in microfluidic channels (Chiu et al. 2013) and design criteria to engineer the hydrodynamically focused streams at Reynolds numbers relevant to microfluidic applications (Nasir et al. 2011) have been reported. In this paper, we use these findings to design and build a microfluidic device for sample preparation capable of removing large debris from a ground beef sample inoculated with live *Listeria monocytogenes* bacteria, a food-borne pathogen and the causative agent of listeriosis disease (Farber and Peterkin 1991). The device combines lateral migration in co-flowing liquid streams (Amini et al. 2012; Nieuwstadt et al. 2011) with 3D hydrodynamic focusing (Chiu et al. 2013) to clean a target sample without using porous membranes. In contrast to previous works that concentrated solely either on the hydrodynamic focusing effect or the lateral migration of the particles, our main focus is the recovery of the target sample stream at the device outlet. In this respect, we present and compare different outlet configurations and pumping protocols with the aim of improving the efficiency in recovering bacteria while removing debris from the initial sample as much as possible. We are interested in evaluating this process in terms of (i) the efficiency of inertial lateral migration effect in removing large debris particles from the beef samples, (ii) recovery efficiency of pathogens in the sample stream and (iii) the degree of interference between the lateral migration and hydrodynamic focusing effects. Various designs are investigated numerically and streamlined by 3D convection-diffusion numerical simulations while actual separation efficiency and target sample recovery at the device outlet are experimentally evaluated by fluorescence microscopy, optical turbidity and bacterial growth measurements.

2 Sample characterization

Extra lean ground beef (Fig. 1a) was combined with phosphate-buffered saline (PBS) to provide a suspension containing a solid mass fraction of 100 mg/mL. The mixture was

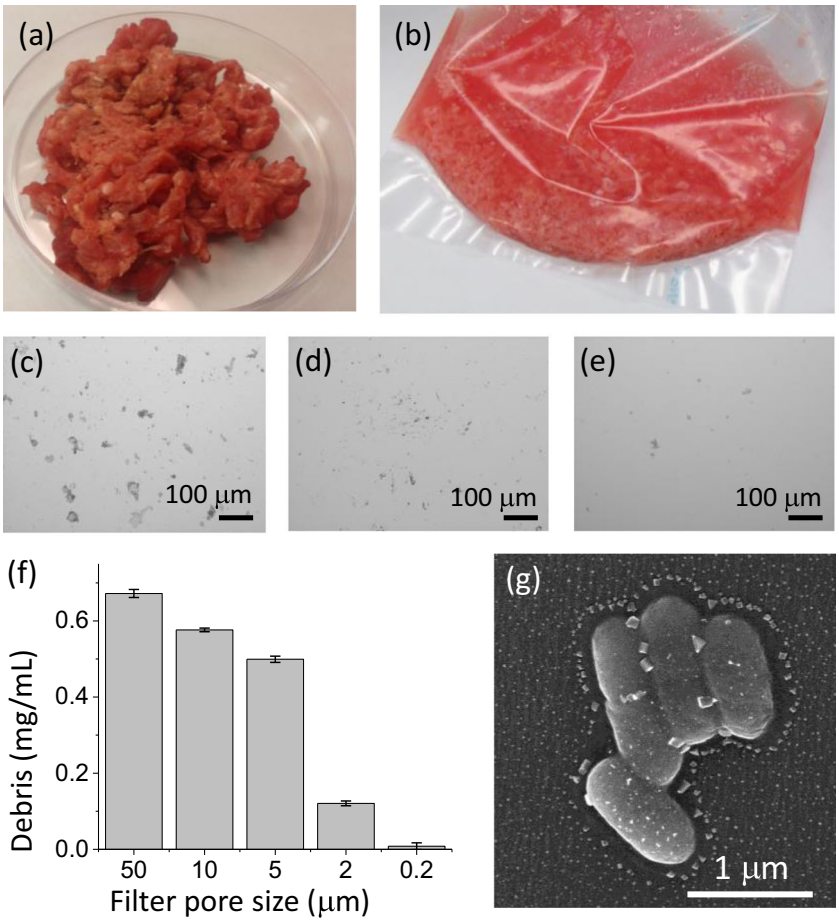

Fig. 1 Sample preparation and composition. **a**) Photograph of the initial solid ground beef sample. **b**) Photograph of a stomacher bag containing a suspension of ground beef in PBS. **c**–**e**) Optical microscope images of debris in the liquid beef sample after filtration with membranes of 50, 20 and 10 μm pore diameter, respectively. **f**) Plot of debris mass density in the filtrate as a function of membrane pore diameter. The data was obtained by optical turbidity measurements. **g**) SEM image of *L. monocytogenes* bacteria on a plastic substrate

subsequently homogenized in a stomacher instrument as described in the Section 4.3. The liquid suspension after homogenization is depicted in Fig. 1b. The sample was then fractionated and passed through membrane filters with pore diameters ranging from 50 to 0.2 μm. The filtrates have been investigated by optical microscopy imaging (Fig. 1c–e) and optical turbidity measurements (Fig. 1f) in order to account for the size distribution of the debris content. The filtrate obtained with a membrane of 50 μm pore diameter contains a solid mass fraction of less than 1 mg/mL (Fig. 1f). We hence conclude that the most part of the debris (99 % of the initial 100 mg/mL) is larger than 50 μm, in diameter making the direct use of any microfluidic technology on these samples impractical. Even after a coarse filtration at 50μm, one still finds large debris (Fig. 1c) that can cause clogging of subsequent microfludic detection instruments. This remaining debris (representing less than 1 mg/mL) is relatively uniformly distributed between 0.2 and 50 μm, though a drastic change in mass density is observed between 5 and 2 μm. However, the removing of the debris content in the sample preparation steps should not entail depletion of species of interest (e.g., *L. monocytogenes*) which must be conserved in the sample stream for further detection and identification steps. *L. monocytogenes* exhibit a rod-like shape with dimensions ranging from 0.4 to 0.7 μm in width and 1.0 to 1.5 μm in length (Fig. 1g). However, since bacteria can easily accumulate and form clusters and chains, filtration of debris up 5 μm, diameter should be avoided to prevent depletion of bacteria in the sample caused by the extraction of these aggregates from the sample stream. In this sense, the microfluidic chip presented herein is adapted for achieving a filtering bandwidth of 7 μm and higher that is considered large enough to avoid depletion of bacteria but at the same time sufficiently low to ensure removal of debris larger than this critical size.

3 General design considerations

Inertial microfluidic devices typically feature relatively long channels in which Reynolds numbers can easily reach values of 10^2 or higher (Di Carlo 2009). Larger Reynolds numbers are required to generate a stable focusing effect within a reasonable channel length. Simple rules for designing inertial microfluidic devices are already well established (Di Carlo 2009; Di Carlo et al. 2007) and rely mainly on the ratio of particle diameter to the channel size as well as the channel Reynolds number.

Several practical implementations of lateral migration effect driven by inertial migration exploit an interesting behaviour of particles flowing in rectangular cross-section channels: at relatively high aspect ratios (depth over width usually >3) particles will preferentially stabilize near the longer (vertical) walls, leaving essentially no particle distributed in the vicinity of the shorter dimension walls (Bhagat et al. 2009). This finding has proven to be very useful in size separation applications since larger particles can be easily extracted from smaller particle admixtures using trifurcated outlets at the end of the separation channels. Combining inertial lateral migration with hydrodynamic focusing at the inlet, specific particles sizes can be directed across streamlines and moved from sample stream to sheath. For example, in devices with a deep microfluidic separation channel of length L and width w with trifurcated inlets and outlets (Fig. 2a) sample mixtures of large and small particles can be introduced through the sample inlet alongside clean buffers injected through two lateral inlet ports. Once in the separation channel, particles larger than a certain critical diameter D_p are focused by lateral migration effect (black dots in Fig. 2a) and pushed towards the lateral walls while smaller ones are flowing unfocused along their streamlines. Several references indicate $D_p \geq 0.07w$ as the critical diameter while practical considerations impose at least few centimetres of channel length for most biological applications (Bhagat et al. 2009; Di Carlo 2009). In this way, larger particles are transferred to the co-flowing sheath flow by the inertial focusing effect and are collected at two side outlets (waste) while smaller particles are collected at the central outlet collector. This behaviour is exploited in the following for cleaning a ground beef sample from large debris transferred by inertial focusing into the lateral flow while smaller target species are maintained into the main stream.

A first objective in the design of such a cleaning device is to ensure that the hydrodynamically focused sample jet does not spread unduly into path and collection of inertially focused debris particles. In other words, the sample stream should remain completely enveloped by the co-flowing sheath along the entire length of the channel. The extent and the position of the focused sample jet are given by the ratio of three flow rates at each of the inlet ports. The cross-sectional shape is also controlled to some extent by the orientation angle of the side sheath channels with respect to the central sample port (Nasir et al. 2011). If we consider debris particles to be focused to about $0.2w$ (20 %) from the channel wall, the lateral dimension of the hydrodynamic sample stream jet must not exceed $0.4w$. Otherwise, these debris particles will not be transferred into the sheath flow but will remain part of the sample stream.

We further investigated the efficiency of recovering the cleaned sample stream at the outlet ports by examining theoretical and practical limitations. Specifically, we designed outlet configurations that provide high efficiency in sample recovery and are compatible with hot-embossing fabrication techniques in polymer materials. A first design consisted of symmetrical inlet and outlet trifurcations based on well-known time-invariant reversible characteristics of flow at low Reynolds number such that a sample jet at the inlet would map exactly and be recovered at the outlet. However, the relatively long channel lengths in inertial focusing devices mean that even at low Reynolds numbers small particle diffusion can become non-negligible leading to cross-

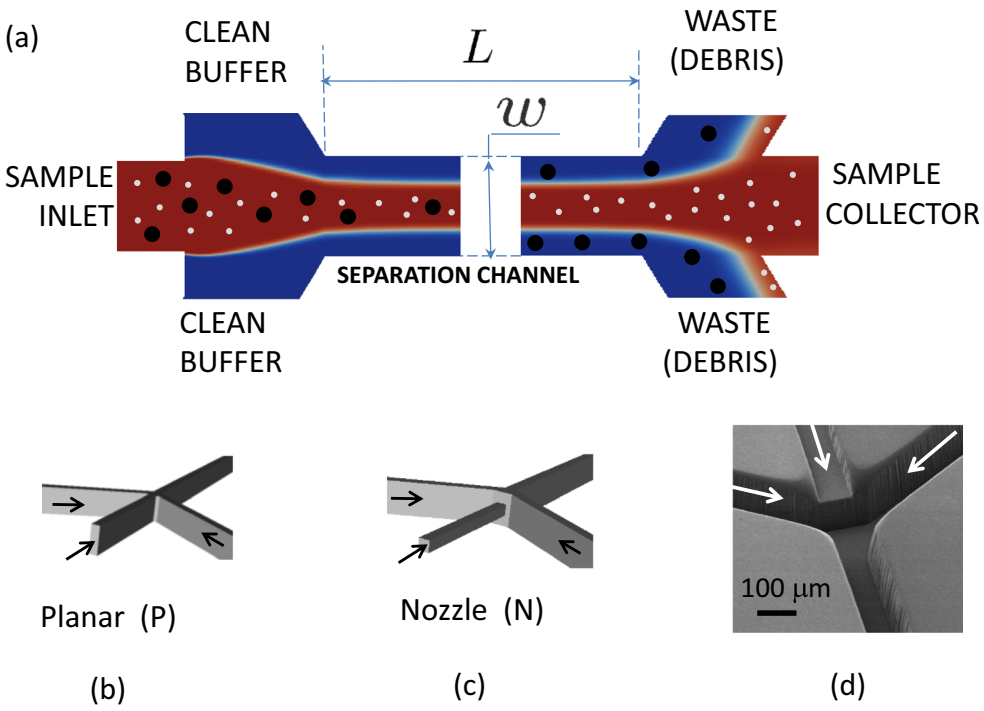

Fig. 2 Chip configuration. **a**) Schematic representation of the microfluidic device containing an inertial focusing channel of length L and width w connected to two trifurcated inlet and outlet access ports. **b**, **c**) Two different configurations for the trifurcations used at the inlet for hydrodynamic focusing and at the outlet for recovery of the sample: P-planar (one level) and N-nozzle (3D), respectively. **d**) SEM image of a hot-embossed plastic microfluidic device with an N-nozzle (3D) type inlet trifurcation

stream drift and sample loss which limit recovery efficiency. Moreover, additional problems could emerge from the practical considerations such as unbalanced or irregular flow induced by debris or air bubbles. For this reason, we also investigate several additional approaches for the recovery of the sample at the outlet.

These configurations are based on two trifurcation constructs shown in Fig. 2b and c: the first is planar (P), consisting of three, same-depth, rectangular channels merging into the separation channel while the second (N) has a smaller central channel or nozzle. Various permutations are then built by capping the separation channel with either P or N type trifurcations. Symmetric configurations combine similar geometries at both ends (such as P→P or N→N) while asymmetric geometries combine the two (such as N→P, for example).

We fabricated microfluidic chips from Mediprene, a commercially available elastomeric styrenic block co-polymer compatible with standard thermoforming techniques such as hot embossing or injection molding (Brassard et al. 2011; Roy et al. 2011) as described in Section 4.1. When subjected to its high-temperature regime, the polymer network softens, allowing material to flow and adapt to the master mould. Subsequent cooling solidifies the elastomer, thus preserving the shape of the imprinted features with high accuracy. Similar to poly(dimethylsiloxane) (PDMS), which is widely used for fabricating microfluidic systems (McDonald and Whitesides 2002), thermoplastic elastomers can form intimate, yet reversible contact with another surface. Conformal adhesion between two layers of Mediprene is strong enough to promote safe, leak-proof manipulation of fluids beyond the specifications provided herein. In addition, Mediprene is optically transparent over a broad range of wavelengths. The overall fabrication process is described in Section 4.1 and involves assembly of two quasi-identical halves (e.g., top and bottom layers) with rectangular geometry measuring 3 and 5 cm in width and length, respectively. A scanning electron microscopy (SEM) image of the bottom half of an N-type (nozzle) inlet region as obtained after hot embossing is shown in Fig. 2d. The assembly process using top and bottom halves allows for both high aspect ratio channel depths and construction of the 3D nozzle features in a single embossing process. The chip retains flexibility which allows for convenient handling and manipulation at all time. Flow rates at both inlet and outlet are controlled individually and independently via a custom-built syringe pump connected to the chip using standard microfluidic tubing.

4 Materials and methods

4.1 Fabrication and assembly

The fabrication of the microfluidic device is schematically depicted in Fig. 3. SU-8 moulds were prepared from

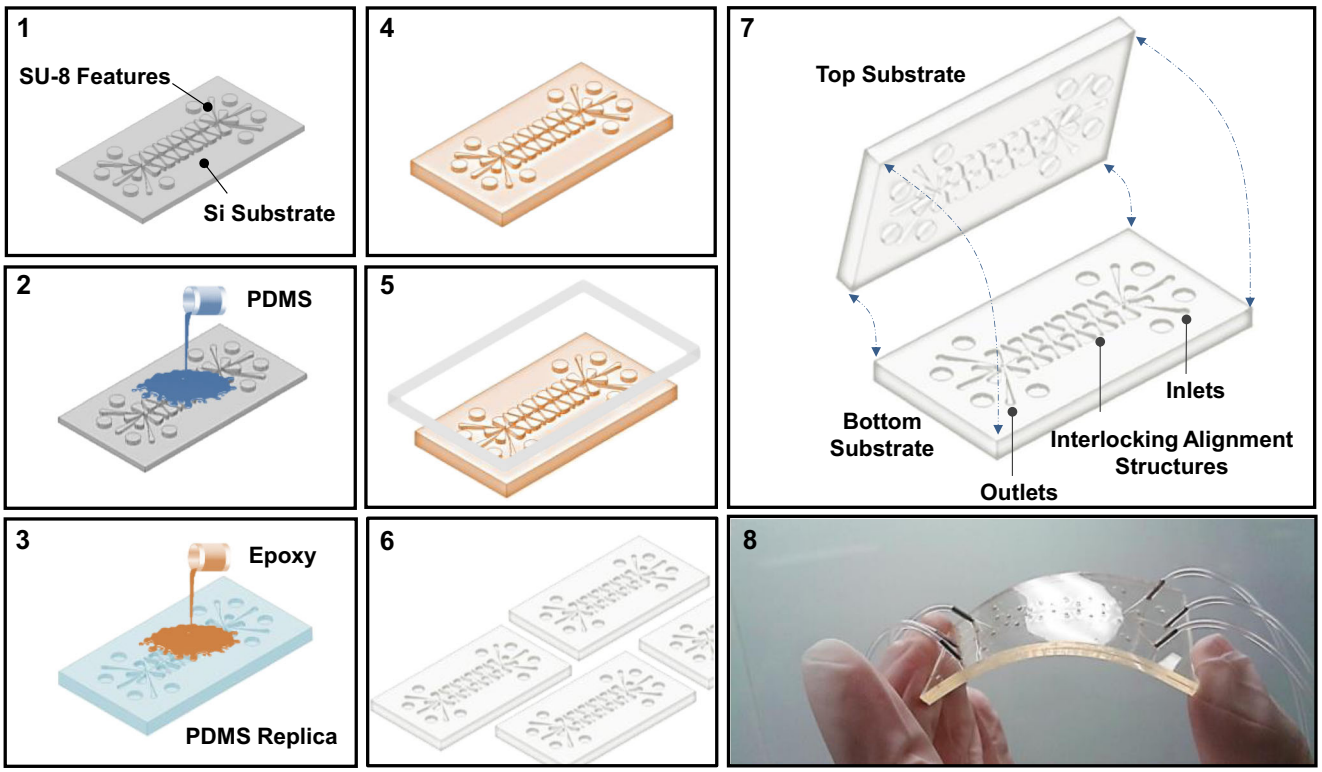

Fig. 3 Fabrication of microfluidic chip by hot embossing and two-half assembling procedure: (*1*) fabrication of SU-8 molds by photolithography; (*2*) mould inversion transfer into PDMS; (*3*, *4*) fabrication of a hard Epoxy mould; (*5*, *6*) hot-embossing of Mediprene; (*7*) assembling of the two-half substrates with interlocking alignment structures; (*8*) photograph of the assembled microfluidic chip

GM1060 and GM1075 (Gersteltec, Pully, Switzerland) on 6-inch silicon wafers (Silicon Quest International, Santa Clara, CA) using standard photolithography. High-definition transparency (mylar) photomasks were obtained from Fineline Imaging (Colorado Springs, CO). Resist was applied by (at least) two consecutive spin-coat deposition cycles, each followed by a pre-bake at 40 °C for 30 min and 120 °C for 2 min in an oven. The resist film was exposed to UV light at 365 nm (Hg i-line), followed by development in propylene glycol monomethyl ether acetate (PGMEA; Sigma-Aldrich, Oakville, ON) for several minutes. The wafer was rinsed with PGMEA and isopropanol (Anachemia, Montreal, QC) and dried with a stream of nitrogen gas. Finally, the mould was hard-baked at 135 °C for 2 min (using a ramp of 2 °C/min). Epoxy molds were fabricated using an intermediate replication process with PDMS (Sylgard 184; Dow Corning, Midland, MI). The liquid prepolymers of PDMS (mixed at a 10:1 ratio of elastomer base/curing agent) were poured onto the master mould followed by curing at 80 °C for 2 h. An epoxy resin (CONAPOXY FR-1080; Cytec Industries, Woodland Park, NJ) was prepared using a 5:4 ratio of resin/hardener followed by degassing under reduced pressure. Once applied to the PDMS mould, the resin was cured at 90 °C for 12 h. Upon removal, the cured epoxy mould was hard-baked at 180 °C for 3 h. Mediprene OF 400M was received in the form of pellets from Hexpol TPE (Elasto, Åmål, Sweden) and was extruded at 165 °C to form sheets of several meters in length and 1.0 mm in thickness. Hot-embossing of these sheets was performed with an EVG 520 system (EV Group, Schärding, Austria) at a temperature of 120 °C. Each half of the device was cut during embossing so that the fluidic units had only to be removed from the mould upon completion of the process. Access holes and were punched in a manual fashion. Alignment features were included in each of the replicated layers to facilitate assembly of the chip during which methanol (Sigma-Aldrich) was used to lubricate and position both substrate halves. The inlets and outlets were then connected via metallic inserts (New England Small Tube Corp., Litchfield, NH) and Silastic laboratory tubing (I.D. 0.76 mm, O.D. 1.65 mm; Dow Corning) to an in-house built syringe pump with independently controllable motors and standard 10 mL syringes (Becton Dickinson and Co., Franklin Lakes, NJ). All fabrication steps were carried out in a clean room (class 1,000) environment.

4.2 Numerical simulations

Numerical simulations are used to investigate diffusive losses at the interface between the sample and the co-flowing sheath for each configuration to evaluate the hydrodynamic focusing at the inlet. The model considers the two liquids (sample and sheath flow) as a two-component liquid flow where the two components are basically water-like. One of the components is considered clean (no particle suspensions) whereas the other can contain species at different concentrations and diffusivity constants. The transport of mass from one component to the other is obtained from the convection-diffusion equation

$$\frac{\partial C}{\partial t} + \nabla\cdot\left(C\vec{U}\right) - \nabla(D\nabla C) = 0 \tag{1}$$

coupled with the Navier–Stokes momentum equation for incompressible flows and Newtonian fluids

$$\rho\left[\frac{\partial\vec{U}}{\partial t} + \left(\vec{U}\cdot\nabla\right)\vec{U}\right] = -\nabla p + \mu\nabla^2\vec{U} \tag{2}$$

These equations are solved with the free open source CFD software OpenFOAM and the built-in solver *twoLiquidMixingFoam* version 2.1.0 (www.openfoam.org). In the above equations C is the concentration of the solution, D is the diffusion constant and U is the velocity field of the flow, while p, p and μ stand for the density of the liquid, the pressure field and the dynamic viscosity, respectively. The two components in the liquid flow have the same density and viscosity (water) but different compositions ($C\neq0$ for the sample flow and $C=0$ for the sheath flow). In order to account for all possible losses from sample stream to the sheath flow, a diffusion constant of $D=10^{-9}\mathrm{m}^2/\mathrm{s}$ was used which corresponds to the self-diffusion of water in water (Tanaka 1978). The computational domain consists of about 10^6 hexahedral elements with volumes uniformly distributed between 4.2×10^{-7} and 2.7×10^{-15} m^3. Using a super-computer equipped with Intel Xeon processors at 2.67 GHz, the above numerical model required close to 10 gigabytes of memory and was able to converge to a steady state solution after about few hundred cpu-hours.

4.3 Sample preparation, inoculation and bacterial growth

For the beef filtrate sample, 25 g of extra lean ground beef was added to 225 mL PBS (pH 7.2; Sigma-Aldrich) for a total of 1 in 10 dilution. The mixture was then homogenized using a Stomacher 400 (Seward, West Sussex, UK) for 2 min at 260 rpm. The suspension was filtered through a 4-inch nylon grid membrane filter with 55 μm pore diameter under vacuum. For the bacteria recovery experiments, three types of samples were prepared. Sample #1 contained the ground beef blended with PBS as described above. Sample #2 consisted of PBS inoculated with live *L. monocytogenes* at a concentration of 10^4 bacteria/mL while sample #3 is the ground beef homogenated in PBS and inoculated with live *L. monocytogenes* at a concentration of 10^4 bacteria/mL (prepared the same day). The

samples were injected through the S_{in} inlet of the microfluidic device, while $B_{1,in}$ and $B_{2,in}$ carried clean PBS at flow rates corresponding to the desired flow profile with the sample outlet biased from 0 to 40 % with respect to the balanced configuration (100 μL/min). For each experimental replicate, 100 μL of the collected solution was plated on RAPID'*L.mono* agar plates (Bio-Rad, Hercules, CA) in triplicates and incubated at 37 °C for 24 to 48 h. Recovery rates and losses are calculated from bacteria count at inlets and outlets.

4.4 Optical turbidity measurements

The optical turbidity of the sample liquids was measured *in-situ* by using optical switches OPB350W062Z (as provided by TT Electronics, Surrey, UK) mounted on Silastic connection tubes with an outer diameter of 1.65 mm. Each optical switch integrates an infrared (IR) light emitting diode (LED) and a phototransistor mounted in a single package so that the LED normally illuminates the phototransistor, though any object inserted in the switch slot will affect the light beam and the phototransistor output. The instrument used for measuring the optical turbidity of a sample flowing through a microfluidic connection tube is schematically represented in Fig. 4a. By using two optical switches (D_1-T_1 and D_2-T_2) and an instrumental amplifier LH0084CD (National Semiconductor, Lewisville, TX), a voltage proportional to the difference in optical transmission of a sample (M) with respect to a clean reference (R) is generated. In the following we describe the procedure for calibrating this instrument for mass density of debris in ground beef samples. This is achieved by comparing optical transmittance to direct mass debris measurements of beef samples filtered at different sizes using membrane filters with 0.25, 2, 5, 10 and 50μm pore diameter. Optical transmittance (T) of several filtrates of ground beef suspensions was recorded on a Lambda 950 UV/Vis Spectrometer from Perkin Elmer (Waltham, MA). Measurements were performed using standard quartz spectrophotometer cells with rectangular geometry (VWR International, Radnor, PA) providing a capacity of 3.5 mL and an optical path length of 10 mm. Spectra were collected between 250 and 1500 nm with a step

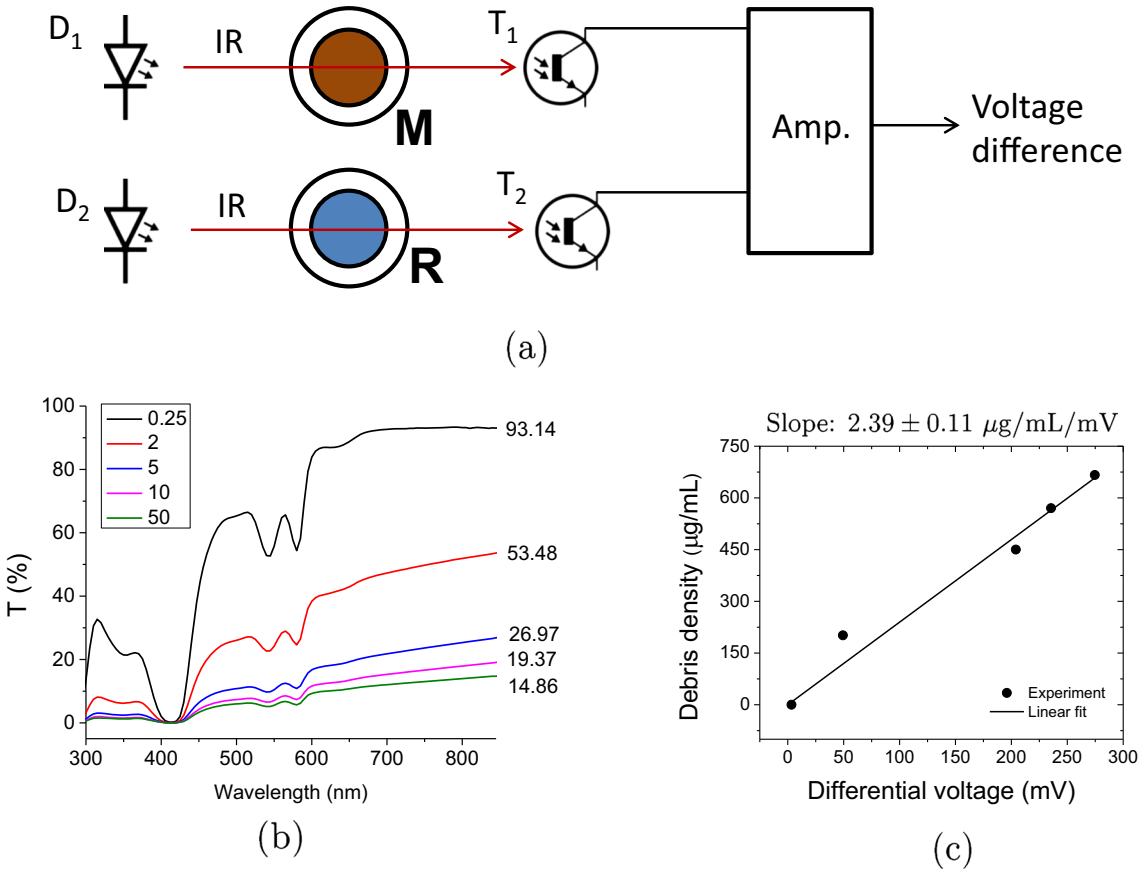

Fig. 4 Sample characterization. **a**) Experimental setup for *in-situ* optical turbidity measurements consisting of two infrared (IR) emitting diodes (D_1 and D_2) coupled to two respective phototransistors (T_1 and T_2) to pass emitted light through the measured sample (M) and reference (R) tubes. The voltage difference at the collectors is amplified by an instrumental amplifier. **b**) Plot of optical transmission spectra as a function of the laser wavelength for different mass fractions of debris obtained through filtration (using membranes with 0.25 to 50 μm pore diameter). Numbers at the end of each curve represent values of transmittance T at a wavelength of 850 nm. **c**) Calibration curve for the actual debris mass density in a sample as a function of the instrument reading voltage (in mV)

width of 5 nm (Fig. 4b). Pure buffer solution was included as a reference for baseline correction. Numbers at the right end of each curve represents the optical transmittance at 850 nm which is the approximate wavelength of the light emitted by the diode in the optical switches. These values are related to the linear attenuation coefficient α through the Beer-Lambert law $I=I_0e^{-\alpha d}$. Then direct mass measurements of the debris in the 50 μm beef filtrate were performed after all the debris was collected with 0.22 μm Millipore filters. In order to eliminate the water, these filter capsules were centrifuged at 10,000 rpm for 10 min and dried in an oven at 80 for few days. The mass density obtained from these measurements is used to determine the mass density of each filtrate by considering $\alpha=k\rho$ that is a proportionality relationship between the linear attenuation coefficient and the mass density of debris. The voltage indicated by the differential amplifier is then plotted against the mass density of the debris and the data interpolated in the least square sense with a regression line (Fig. 4c). In this way we find that the average sensitivity of our *in-situ* turbidity instrument is 2.39±0.11 $\mu g \cdot mL^{-1}mV^{-1}$.

5 Results and discussion

5.1 Numerical simulations

The numerical model described in Section 4.2 was used to perform numerical simulations of different configurations of the microfluidic chip. For all configurations the flow rates al all three inlet channels have been set to 100 μL/min giving a total flow rate of 300 μL/min in the main separation channel. It has been shown previously (Chiu et al. 2013) that the N-type structure performs better in hydrodynamic focusing (and maintaining) the sample stream along the separation channel than the P-type structure. In a P-type configuration, the sample stream is in direct contact with the top and bottom channel walls (Fig. 5a-1) where the flow velocity is low and loss through diffusion is important. Consequently, the sample stream can become significantly depleted, this phenomenon being known in the literature as the "butterfly effect" (Ismagilov et al. 2000; Kamholz and Yager 2001). For example, Fig. 5a-2 shows a drastic reduction in sample concentration at a point 3 cm downstream along the separation channel. Beyond that the concentration profile along the channel axis drops to below 60 % of its initial value at the inlet.

In contrast, when the N-type nozzle configuration is used this problem is circumvented because the sample stream is completely surrounded by the sheath liquid (Fig. 5a-3). The presence of the sheath flow around the sample ensures that the sample stream is well maintained in a region of high liquid flow velocities that minimize diffusive losses along the channel (Fig. 5a-4). The breadth of the hydrodynamic jet within the

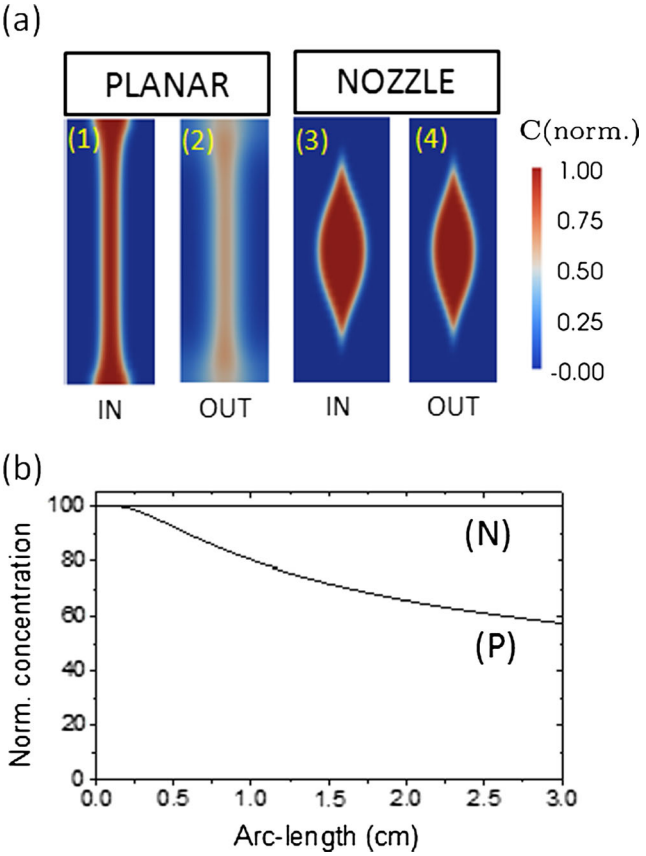

Fig. 5 Numerical simulation of the hydrodynamic focusing effect. **a**) Contour fill plots for the hydrodynamically focused streams generated by the planar (P) and the nozzle (N) structures at the beginning and the end of the respective separation channels. **b**) Plot of the concentration profile along the separation channel for P and N configurations

channel largely depends on the flow rates at the three inlets while its shape is influenced by the channel aspect ratio, the angle of confluence of the trifurcation branches and the Reynolds number (Nasir et al. 2011). Since we seek to build cleaning devices that remove particles and debris larger than ~ 7 μm, a separation channel of 100 μm in width and at least few centimeters in length (Bhagat et al. 2009; Di Carlo et al. 2007) is necessary. Moreover, to focus all large debris along the vertical (long) walls only, a large aspect ratio for the separation channel cross-section profile is mandatory. To this end, the hot embossing fabrication method described in this paper easily replicates aspect ratios of 3 (or even more) by employing the two-half assembly and self-alignment procedure as discussed in detail in the Section 4.1.

Considering these practical constraints and an angle of confluence of 120° between lateral branches and the separation channel as recommended elsewhere (Nasir et al. 2011), the contour of the hydrodynamically focused sample stream has an oval cross-sectional shape (Fig. 5a-3) with smaller radius of curvature at both top and bottom parts. Focused segments cover about 64 % of the total channel depth and 49 % of the width. Diffusion losses along the

separation channel are minimal as we can observe in Fig. 5b (the curve N). Therefore, the nozzle configuration is used throughout the following as the microfluidic inlet of choice.

Next, the configuration of the outlet must be designed to optimally collect the sample and the sheath flows with maximum efficiency while avoiding cross contamination. Among the different available design configurations, the N→N and N→P are of most interest. Numerical simulations of the hydrodynamic focusing effect in each of the different configurations show very different behaviour at the outlet. Contour fill plots of concentration at the outlet trifurcation in the plane perpendicular to the flow (Fig. 6a-c) indicate a clear mismatch between the jet cross-sectional profile and the various sample outlets (as indicated by dashed rectangles in this figure). The integral of the concentration profile over the surface of these dashed rectangles is related to the recovery rate of the mass flux at the sample outlet port. Accordingly for P→P devices, a modest value of 48.9% of the initial mass flux is recovered, that is more than 50% of the sample is lost to the sheath flow. This important loss originates from diffusive loss along the separation channel (as discussed previously) and the subsequent mismatch between the profile of the sample stream and the outlet port (Fig. 6a). For the case of a P→N device (terminated in an N-type nozzle configuration) the situation is exacerbated with further reduction in the recovery rate as the extraction channel does not sample evenly the entire vertical extent of the sample, providing a clear argument to dismiss this design as impractical for separation purposes. Consequently, when a P-type planar trifurcation is used as an inlet, no more than 50 % of the original sample can be extracted at the outlet port.

In contrast, the use of an N-type nozzle structure as an inlet is advantageous because it preserves the sample in a very compact region with minimal diffusive losses along the separation channel. Despite this conservation, there still remains a mismatch between the profiles of the hydrodynamic sample jet and the cross-section of the extraction channel (Fig. 6b and

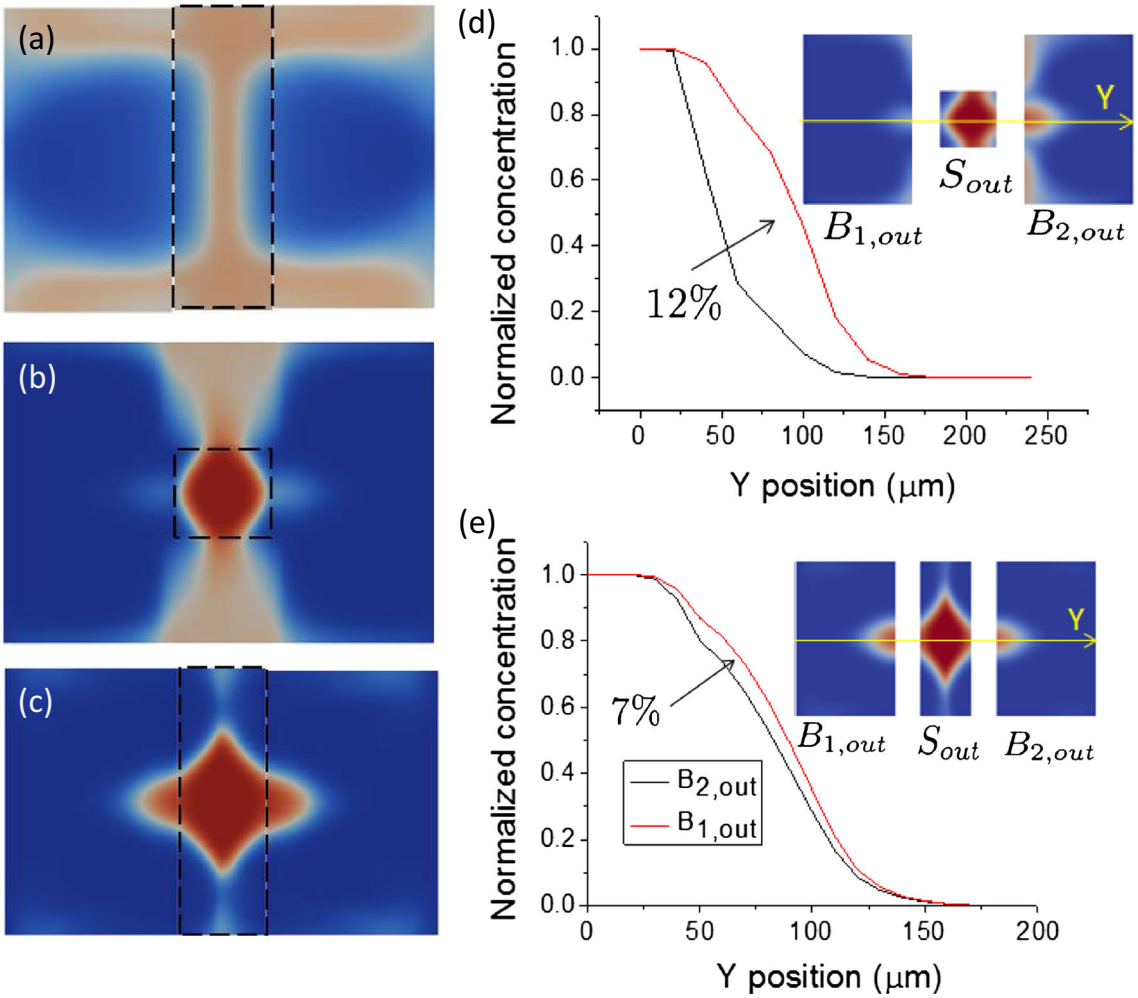

Fig. 6 Contour fill plot of the sample concentration at the outlet for P→P (**a**), N→N (**b**) and N→P (**c**) configurations. Profile of the central sample extraction outlet channel is indicated with *dashed squares*. **d**–**e**) Concentration profiles along outlet in-plane direction (Y) when the flow in one lateral branch ($B_{2,out}$) is increased by 10 % with respect to the other lateral branch ($B_{1,out}$)

c). The integration of the mass flux over the outlet cross-sectional area gives a recovery efficiency of 82.8 % for N→N (Fig. 6b) and 79.5 % for N→P (Fig. 6c). As expected, the use of a nozzle at the inlet improves outlet recovery by at least 30 % over the simple "planar" counterpart. The symmetric structure N→N having nozzle both at the inlet and the outlet is marginally better, giving a 3 % higher recovery rate than N→P. However, as shown below, there are several practical considerations that point to the N→P configuration as a viable design along with or even instead of the symmetrical N→N.

First, the overall hydraulic resistance of the N→P design is significantly lower because the central output channel is deeper than in the constricted N→N design. This can be decisive for already high impedance, small diameter separation channels (for inertial focussing, channel widths are approximately 10 times the particle diameter to be focused). Driving pressures necessary to maintain sufficiently rapid flows for inertial migration can easily go in the order of tens of atmospheres in these channels if submicron particles are to be focused.

Secondly, from a more practical point of view, the bottleneck created by an outlet nozzle can cause accumulation of debris and even device clogging. Avoiding this issue is of critical importance in sample preparation applications (e.g., to extract target bacteria from contaminated food samples) where the device is used to filter out large debris from a relatively dirty sample while keeping the sample stream as intact as possible.

Finally, the numerical simulations also demonstrate that the N→P configuration is less sensitive to unbalanced flows than the N→N termination such as when flow rate fluctuations are present in the two side outlet buffer channels. Several factors including fabrication issues, formation of air bubbles and accumulation of debris can cause unbalanced outlet flows. These factors change the hydrodynamic resistance locally causing differential flow rates across the three outlets. By changing the outlet boundary conditions in the numerical simulation we investigated the effects of these variations on the distribution of mass concentration. For example, a 10 % increase in flow rate on one side of an N→N debris collection channel results in a 12 % difference in mass flux across the horizontal plane at half length of the trajectory (Fig. 6d). For the N→P case the same 10 % unbalance results in only a 7 % reduction in mass flux (Fig. 6e). These values are simply calculated by integrating the mass concentration profiles along the Y axis (as indicated in the respective insets). If we also take into account losses near the top and bottom walls of the side channels (inserts of Fig. 6d and e), mass flux losses analysis further favours the N→P design. However, as the channel aspect ratio increases, these marginal losses will have less impact on the overall efficiency becomes closer to those calculated for results in Fig. 6d and e. Nevertheless, an N→P configuration will be considered as the best option for the experimental investigations described hereafter.

Another avenue towards improving the sample recovery rate is to intentionally increase the flow rate at the central sample collector with respect to the sheath collector channels. This approach will cause the final sample volume to be slightly larger than the initial one as some buffer liquid will be artificially added to the sample. Benefits and limitations to this approach will be analyzed in the following sections with respect to lateral migration and recovery rate.

5.2 Calibration with fluorescent beads

In a first experiment, a mix of spherical particles that are 1 and 15 μm in diameter is injected through the sample inlet of an N→P device at a flow rate of 100 μL/min while a clean buffer solution (water) is injected through the side channels at the same flow rate. Both inlet and outlet trifurcations are visualized with the help of a fluorescence microscope and images featuring the trajectories of the fluorescent beads are constructed by integrating the fluorescence intensity over 200 recorded camera frames (Fig. 7a). As revealed in these images, the hydrodynamic jet is well formed at the inlet (left) while larger 15 μm particles (visualized in green) are correctly extracted from the mixture into the outlet sheath flow collector channels (right). However, although less visible in the integrated image of the outlet in Fig. 7a, some of the small particles are still transferred to the lateral outlet buffer ports. This is obviously due to imperfections in both fabrication and local flow unbalances but to the diffusion of small particles as well. For particles of 1 μm diameter and a transition time along the microfludic channel of 0.3 s, a diffusion length ι_D of about 1 μm can be obtained by using the Stokes-Einstein relation. For *L. monocytogenes* bacteria whose diameters d can be even smaller (Fig. 1f), these diffusion effects can become larger as the diffusion length scales to the particles diameter according to $l_D \propto 1/\sqrt{d}$.

As proposed earlier, a possible path to minimize these losses would be to unbalance the flow rates in favour of the central outlet by drawing more liquid through this port. A similar strategy would be to reduce the size of the hydrodynamic sample jet by diminishing the flow rate at the sample inlet port and keeping the outlet port well balanced. However, while the recovery rate can be increased through the central outlet port, there is a risk of diminished filtration efficiency as larger particles, initially focused by the inertial migration effect, can also be drawn from their positions along the side walls closer to the channel centre, that is in the region corresponding to the central outlet supposed to be free of large debris. A very quick estimation of this limit can be made by

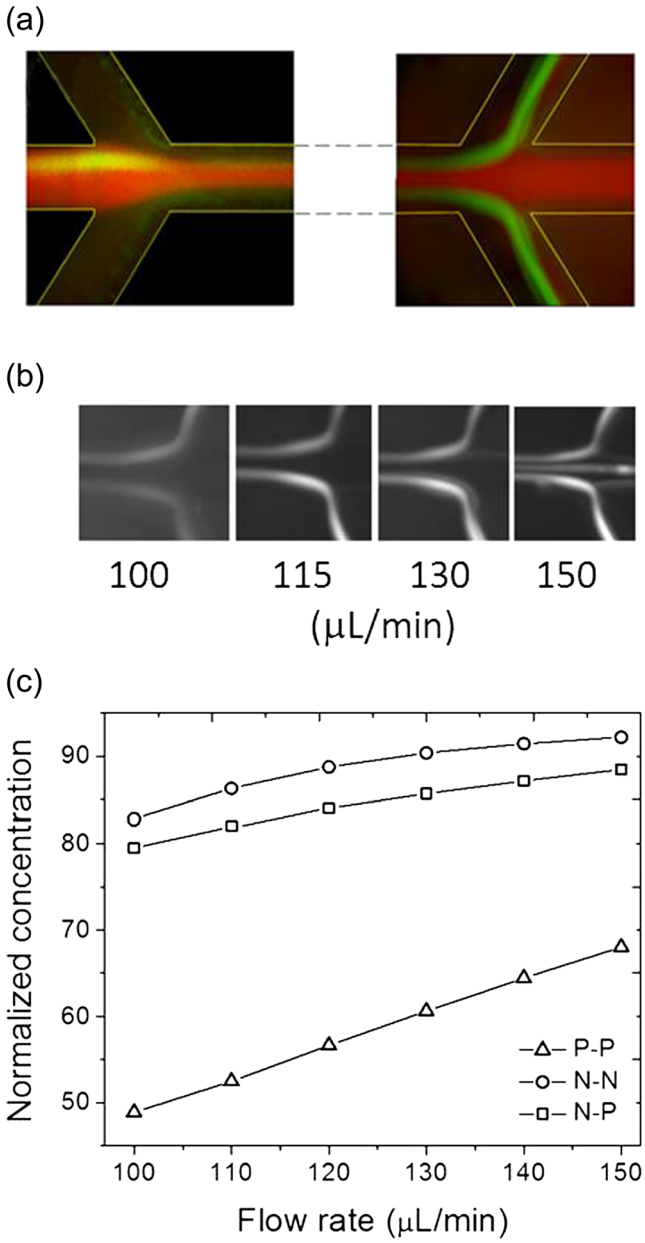

Fig. 7 Size-dependent separation with a binary mixture comprising particles that are 15 μm (*green*) and 1 μm in diameter (*red*), respectively. **a**) Fluorescence microscopy images of the hydrodynamic jet at the inlet (left) and outlet trifurcation (right). **b**) Fluorescence microscopy images of inertial focalisation of large particles at the outlet for different flow rates at the central outlet. **c**) Theoretical simulation of the sample recovery rate for different flow rates at the central outlet

considering the flow rate associated with the fluid region between the inertial focusing positions (20 %, for example) and the limits of the central sample flow (38.7 %) that is about 18.7% of difference for one side only. This gives a maximum allowed flow rate increase of 37.4% at the central outlet before debris is drawn back into the sample stream. To verify this number, we performed several experiments with fluorescent beads where the flow rate at the central outlet is increased gradually from 100μL/min to 150μL/min while the total flow rate at lateral outlets is diminished such that the total flow rate is always 300μL/min (Fig. 7b).

We observe that at low unbalance rates the inertially focused particles behave similarly to the situation depicted in Fig. 7a in the sense that they are focused by the separation channel and properly collected at the side outlets. At these flow regimes, the behaviour of the spheres is well preserved and the central outlet is free of large particles (simulating debris). However, at 50 % flow rate increase at central outlet, 75μL/min on sides), green fluorescent beads deviate from the lateral focus positions and migrate toward the channel centre and are unavoidably captured in the central outlet. These results confirm that the upper limit for a debris-free central outlet is between 30 and 50 % flow rate bias (130μL/min and 150μL/min, respectively) as predicted by the above simple analytical calculations. The following section details a theoretical investigation of the recovery rate for unbalanced collection flows.

5.3 Theoretical recovery rate

To investigate recovery efficiencies obtained by deliberate outlet flow imbalances, we first performed a series of numerical simulations where boundary conditions at the outlet channels were changed to account for flow rate variations at the central outlet of up to 50 % with respect to the initial balanced value of 100 μL/min (as in the previous experiment with large fluorescent beads). As explained above, the recovery rates are calculated at different flow rates by integrating the mass flux over the transversal area of the outlet sample channel. Examples are plotted in Fig. 7c where N→N and N→P configurations are represented by empty circles and squares, respectively (the configuration P→P is included as well for informative and comparison reasons).

At a first glance, recovery improvements for the P→P configuration appears promising, rising by about 15 % for increasing central channel flow rates of 100 to 150 μL/min, but overall, efficacy for this configuration remain very low at less than 70 % since the sample is spread almost everywhere into the channel.

In contrast, the N→N and N→P configurations give initial recovery rates starting at 80 %, improving an additional 5 % for a central channel flow rate of 150 μL/min (75μL/min on side channels). However, as noted previously, imbalances >30 % increase the probability of sample re-contamination from recently separated large particles. From the results plotted in Fig. 7c we observe that theoretical recovery rates between 80 and 90 % can easily be obtained within this limit.

These figures of merit will be evaluated for the N→P configuration using real food samples. Here, larger particles are actual food debris quantified *in-situ* by optical turbidity measurements. Meanwhile, the smaller target particles for cleaning and collection are live

L. monocytogenes bacteria counted by bacterial growth measurements.

5.4 Removal of debris

We evaluated the performance of the device in removing debris from the main sample stream using ground beef in PBS (sample #1 prepared as described in Section 4.3). The suspension was first coarsely filtered using nylon grid membranes with a 50 μm pore diameter to prevent the microfluidic chip from clogging. This sample was then injected along with PBS buffer through the central and lateral inlet ports, respectively, using a syringe pump. Similarly, the liquids are recovered at the outlet ports using three additional syringes (as shown in Fig. 2e). The flow rate at each port was set independently to 100 μL/min. For the tubing used for connecting the chip to the syringe pump is optically transparent, we were able to monitor the passing solution with optical sensors to evaluate sample turbidity (as described in Section 4.4).

Measurements of raw samples injected at the central inlet port indicate a debris mass density between 400 and 700 μg/mL. As expected, sample-to-sample variability is observed, which we attribute to the inherently inhomogeneous nature of the beef sample content. On the outlet side, when the flow rates at the three ports are perfectly balanced (100 μL/min at each outlet) we observe that ~55 % of the mass of debris in the sample are transferred to the lateral outlets, meaning that more than half the mass of debris is removed from sample stream (Fig. 8a). However, the sample characterization based on optical turbidity measurements in Fig. 1f indicates that the concentration of debris larger than 5 μm is less than 50 % in the sample which can be evaluated from the graph by the difference in average mass density for filters with 50 and 5 μm pore diameter. This apparent contradiction can be explained by the fact that most part of the debris particles are irregular in shape (Fig. 1c-e) and their hydrodynamic radius responsible for inertial focusing effect (Hur et al. 2011) is actually larger than the bandwidth of the porous membranes that is basically defined by the smallest size of the particles.

Unbalancing the central outlet port with gradually larger flow rates leads to increased turbidity at the central sample collection port. As a result, solid mass fraction increases for the sample outlet while less debris is extracted to the lateral ports by inertial focusing. However, at 30 % flow rate bias (130 μL/min at the center and 85μL/min on sides) we are still able to transfer about 40 % of the debris out of the sample stream while retaining 60 % of mostly small debris particles (Fig. 8a).

5.5 Recovery of bacteria

The efficiency in recovering *L. monocytogenes* bacteria at the sample outlet is measured first in PBS (sample #2) and then in ground beef filtrate (sample #3) by counting bacteria cells at central inlet and all three outlet ports (preparation methods for sample #2 and #3 are described in Section 4.3). Sample recovery efficiency is evaluated then as the percentage of the bacteria counted at the central outlet with respect to the overall counts at all three outlet ports. In clean PBS samples and balanced pumping configuration (no flow rate bias), 90 % of the bacteria are recovered at the outlet while the remaining 10 % are collected in the buffer outlets as a result of corroborate diffusive and manipulation losses. A general trend towards increased recovery efficiencies is observed as the flow rate at the sample outlet is increased. This efficiency approaches 100 % when the sample outlet flow rate is biased from 100 μL/min to 140 μL/min. Little to no loss associated with non-specific absorption on channel walls is observed due to the inlet nozzle configuration. Efficacy is slightly better in this case than that predicted by numerical simulations. The reason for this difference is that the numerical simulations consider a diffusion constant corresponding to the self-

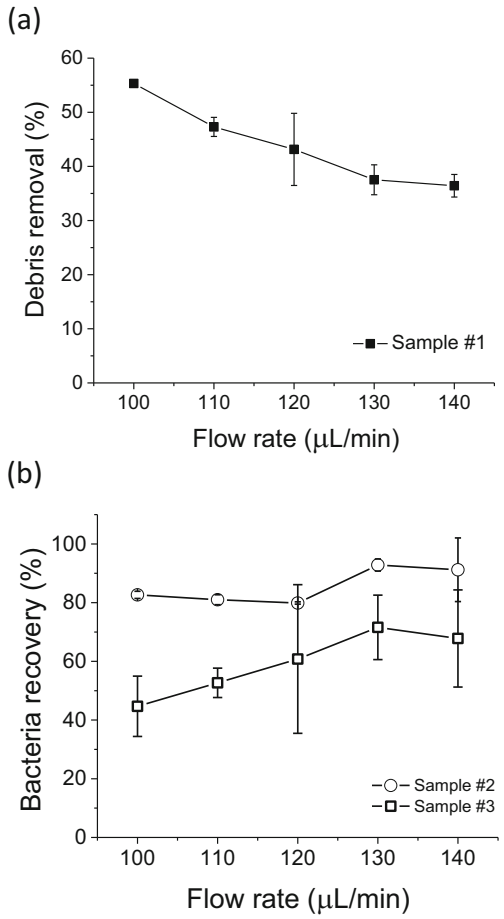

Fig. 8 Efficiency of inertial microfluidic filtration in food samples. **a**) Efficiency of debris removal at lateral waste ports as obtained from *in-situ* turbidity measurements of sample #1 (beef) at different flow rates. **b**) Bacteria counts at the central outlet port for sample #2 (bacteria inoculated PBS) and #3 (bacteria inoculated beef)

diffusion of water ($D=10^{-9}$ m^2/s) while the bacteria diffusion is at least few orders of magnitude smaller ($D=4.4\times10^{-13}$ m^2/s for 1 μm diameter).

Finally, we explore the possible interference between lateral migration and the hydrodynamic focusing effects. Using the sample #3, we evaluate the recovery efficiency of *L. monocytogenes* for the inoculated beef filtrate. Given the previously measured recovery losses, the experiment was carried out only for flow rate biases up to 140 μL/min (40 %). As shown in Fig. 8b, the bacteria recovery rates measured at the sample outlet are lower than those measured in PBS and now range from 45 % in perfectly balanced flows to 70 % as the bias is increased. The lower recovery rates of the beef filtrate sample compared to that of PBS suggests that the lateral migration of debris entails extraction of some bacteria from the central stream into the lateral sheath flow contributing to the depletion of target pathogens in the sample. Overall, we found a difference of about 15 to 20 % in bacteria recovery between the two cases due to this interference. In addition to hydrodynamic effects generated by streamline crossing of rotating large debris during inertial lateral migration toward the walls, (Amini et al. 2012; Ismagilov et al. 2000) the natural tendency of bacteria to attach to surfaces (Boland et al. 2000) (i.e., beef debris) may also contribute to this finding. A more detailed investigation of these effects, however, is beyond the scope of this study.

6 Conclusions

In this work, we present, for the first time, a systematic study on the effect of inlet/outlet configuration and flow rate profiles on the performance of an inertial focusing device for the recovery of small particles as well as bacteria from a complex food sample. In particular, we sought to evaluate the interplay between the lateral migration of small particles and the hydrodynamic inertial effects of larger particles. The results obtained from our studies suggest that nozzle inlets with a planar trifurcation design can effectively shield the sample hence preventing loss of target species due to non-specific adsorption. Moreover, this configuration can ensure both a more stable inertial separation and an outlet that is less sensitive to flow rate fluctuations. By balancing debris cleaning with recovery efficiencies, we can conclude that the microfluidic chip presented here is capable of removing more than 50 % of the debris in (pre-filtered) ground beef samples while maintaining up to 70 % recovery of initial pathogenic content at the device outlet. Variation around these values is possible in unbalanced flows but any increase in recovery efficiency will translate into a decrease in the cleanliness of the sample and vice versa. Due to the complex nature of the sample fluid and debris constituents, the removal of the debris into a buffer stream by inertial focusing lead to a significant (20 %) loss of bacteria recovery in the central outlet port. This effect can be redressed to a certain extent by biasing the flow rate of the sample port with respect to the flow rate of the waste ports. While initial focusing devices have been demonstrated to efficiently fractionate suspended particle mixtures, the introduction of complex samples requires an appropriate design of the device and an adequate pumping scheme to ensure acceptable performance. The use of a thermoplastic elastomer in conjunction with hot embossing lithography enabled the fabrication of microfluidic systems in a time- and cost-effective manner, which is, in principle, amenable to mass production of single-use devices. The integration of interlocking structures proved valuable to achieve alignment of complementary parts in the assembly process, accounting for a high degree of reliability in the functioning and performance of the chip. In this way, it was equally possible to attain the 3D, high-aspect ratio microfluidic conduits that are vital to filtration based on hydrodynamic focusing and lateral inertial migration. We believe that the methodology has the potential to support sample preparation in areas such as food safety inspection, environmental screening or clinical diagnostics where isolation and concentration of microbial organisms (e.g., bacteria, parasites or fungi) is of primary concern.

Acknowledgments We thank Dr. Franco Pagotto and Karine Hébert (Health Canada) for providing us with the *Listeria* strain used in this study, Dr. Virginie Barrère, Dr. Geneviève Marchand and Dr. Dominic Lambert (Health Canada) for critical review of the manuscript, and Hélène Roberge (NRC) for SEM imaging. We also thank Réseau québécois de calcul de haute performance (RQCHP) for providing computational facilities. This study was co-funded by Health Canada and the National Research Council of Canada.

References

H. Amini, E. Sollier, W.M. Weaver, D. Di Carlo, Proc. Natl. Acad. Sci. U. S. A. **109**(29), 11593–11598 (2012)

A.A.S. Bhagat, S.S. Kuntaegowdanahalli, I. Papautsky, Microfluid. Nanofluid. **7**(2), 217–226 (2009)

T. Boland, A.R. Latour, F.J. Stutzenberger, *Handbook of bacterial adhesion: principles, methods and applications* (Humana Press, Totowa, 2000)

D. Brassard, L. Clime, K. Li, M. Geissler, C. Miville-Godin, E. Roy, T. Veres, Lab Chip **14**, 4099–4107 (2011)

Y.-J. Chiu, S.H. Cho, Z. Mei, V. Lien, T.-F. Wu, Y.-H. Lo, Lab Chip **13**(9), 1803–1809 (2013)

L. Clime, B. Le Drogoff, S. Zhao, Z. Zhang, T. Veres, Int. J. Nanotechnol. **5**(9–12), 1268–1305 (2008)

D. Di Carlo, Lab Chip **9**(21), 3038–3046 (2009)

D. Di Carlo, D. Irimia, R.G. Tompkins, M. Toner, Proc. Natl. Acad. Sci. U. S. A. **104**(48), 18892–18897 (2007)

A. Escarpa, Lab Chip (2014). doi:10.1039/C4LC00172A

J.M. Farber, P.I. Peterkin, Microbiol. Mol. Biol. R. **55**, 476–511 (1991)

M. Geissler, S. Isabel, B. Voisin, C. Fauvel, M. Boissinot, M. G. Bergeron, T. Veres, J. Bioterr. Biodef. 3, 119-111-116 (2012).

S.C. Hur, S.-E. Choi, S. Kwon, D. Di Carlo, Appl. Phys. Lett. **99**(4), 044101 (2011)
S. Isabel, M. Boissinot, I. Charlebois, C.M. Fauvel, L.-E. Shi, J.-C. Levesque, A.T. Paquin, M. Bastien, G. Stewart, E. Leblanc, S. Sato, M.G. Bergeron, Appl. Environ. Microbiol. **78**, 1505–1512 (2012)
R.F. Ismagilov, A.D. Stroock, P.J.A. Kenis, G. Whitesides, H.A. Stone, Appl. Phys. Lett. **76**(17), 2376–2378 (2000)
A.E. Kamholz, P. Yager, Biophys. J. **80**, 155–160 (2001)
L.A. Kuznetsova, W.T. Coakley, Biosens. Bioelectron. **22**(8), 3883–3892 (2007)
B.H. Lapizco-Encinas, B.A. Simmons, E.B. Cummings, Y. Fintschenko, Anal. Chem. **76**(6), 1571–1579 (2004)
W.W.-F. Leung, *Centrifugal separation in biotechnology* (Elsevier/ Academic Press, Oxford, 2007)
D.V. Lim, J.M. Simpson, E.A. Kearns, M.F. Kramer, Clin. Microbiol. Rev. **18**, 583–607 (2005)
M. Madou, J. Zoval, G. Jia, H. Kido, Annu. Rev. Biomed. Eng. **8**, 601–628 (2006)
D. Mark, S. Haeberle, G. Roth, F. von Stetten, R. Zengerle, Chem. Soc. Rev. **39**, 1153–1182 (2010)
J.C. McDonald, G.M. Whitesides, Acc. Chem. Res. **35**, 491–499 (2002)
M. Nasir, D.R. Mott, M.J. Kennedy, J.P. Golden, F.S. Ligler, Microfluid. Nanofluid. **11**(2), 119–128 (2011)
S. Neethirajan, I. Kobayashi, M. Nakajima, D. Wu, S. Nandagopal, F. Lin, Lab Chip **11**, 1574–1586 (2011)
H.A. Nieuwstadt, R. Seda, D.S. Li, J.B. Fowlkes, J.L. Bull, Biomed. Microdev. **13**(1), 97–105 (2011)
E. Roy, M. Geissler, J.-C. Galas, T. Veres, Microfluid. Nanofluid. **11**, 235–244 (2011)
P.G. Saffman, J. Fluid. Mech. **22**(2), 385–385 (1965)
P.G. Saffman, J. Fluid. Mech. **31**(1), 624–624 (1968)
G. Segre, A. Silberberg, Nature **189**, 209–209 (1961)
K. Tanaka, J. Chem. Soc. Faraday. Trans. **1**(74), 1879–1881 (1978)
H. Wei, B.-H. Chueh, H. Wu, E.W. Hall, C.-W. Li, R. Schirhagl, J.-M. Lin, R.N. Zare, Lab Chip **11**(2), 238–245 (2011)